

Absolute frequency measurement of the $6s^2\ ^1S_0 \rightarrow 6s6p\ ^3P_1\ F = 3/2 \rightarrow F' = 5/2$ ^{201}Hg transition with background-free saturation spectroscopy

ADAM LINEK*, PIOTR MORZYŃSKI, AND MARCIN WITKOWSKI

*Institute of Physics, Faculty of Physics, Astronomy and Informatics, Nicolaus Copernicus University,
Grudziądzka 5, PL-87-100 Toruń, Poland*

**a.linek@doktorant.umk.pl*

Abstract: We report the development of a method for eliminating background-induced systematic shifts affecting precise measurements of saturation absorption signals. With this technique, we measured the absolute frequency of the $6s^2\ ^1S_0 \rightarrow 6s6p\ ^3P_1$ transition in ^{201}Hg ($F = 3/2 \rightarrow F' = 5/2$) to be 1181541111051(83) kHz. The measurement was referenced with an optical frequency comb synchronized to the frequency of the local representation of the UTC. This specific atomic line is situated on the steep slope of the Doppler background at room temperature, which results in a frequency systematic shift. We determined the dependence of this shift on the properties of both the spectral line and the background of the measured signal.

© 2022 Optica Publishing Group under the terms of the [Optica Publishing Group Publishing Agreement](#)

1. Introduction

Saturation spectroscopy is a powerful Doppler-free technique providing detailed information about the electronic structure of atoms through very precise frequency measurements of the atomic transitions. The method is the basis for various laser frequency stabilization and locking techniques [1–7]. The saturation spectrum’s high-frequency resolution is achieved thanks to a significant reduction of the Doppler broadening. However, the spectral lines obtained with the Doppler-free saturation spectroscopy are often situated on a non-flat Doppler background, which limits the precision of the measurements. This limitation is because the signal’s maximum no longer corresponds to the atomic transition frequency. This frequency shift is usually estimated from the fit to the measured line and background profiles. Such treatment is sufficient enough for high-quality data and fitting models. However, the low signal-to-noise ratio measurements result in high uncertainties of the fitting parameters, which makes this method inefficient.

In this paper, we present a novel method stemming from saturation spectroscopy but modified by employing a new way to deal with the undesirable background-induced systematic shift of the atomic transition frequency. The technique is fairly insensitive to temperature changes, which entail changes in the Doppler profile and, thus, in the shape of the measured signal’s background. Using this method, we measured the absolute frequency of the $6s^2\ ^1S_0 \rightarrow 6s6p\ ^3P_1$ transition in ^{201}Hg ($F = 3/2 \rightarrow F' = 5/2$) with a room-temperature mercury vapor cell. This line lies on the steep slope of the Doppler profile at room temperature (Fig. 1), which made it possible to exploit the method’s advantages fully. The uncertainty budget of the measurement includes all significant frequency shifting effects such as AC-Stark, Zeeman shift, and pressure-dependent collisional shift.

The study of spectral lines of mercury has been a subject of interest for over a century [8–16]. Although the mercury’s intercombination $^1S_0 \rightarrow ^3P_1$ line has been the subject of numerous spectroscopic studies (this applies mainly to isotope ^{198}Hg), the $F = 3/2 \rightarrow F' = 5/2$ ^{201}Hg transition, to our knowledge, has not been measured directly. There were, however, reported results [11] of its isotope shift relative to ^{198}Hg (measured in [17]), from which one can

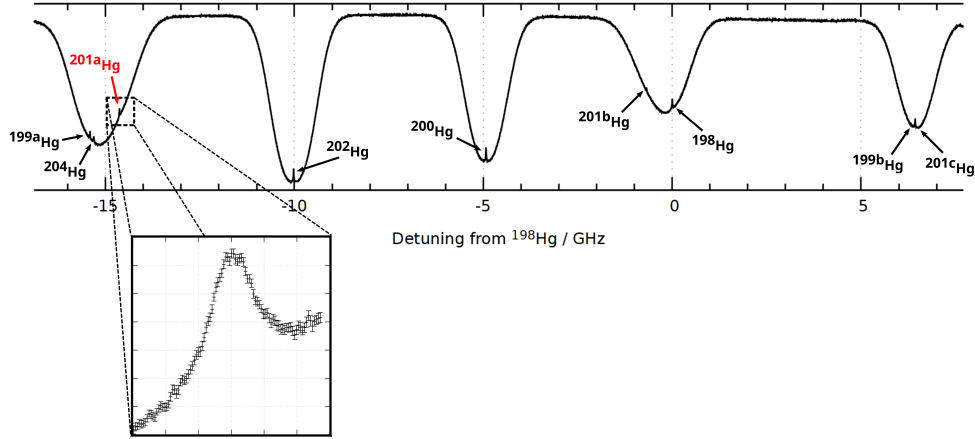


Fig. 1. The saturation spectroscopy of the $^1S_0 \rightarrow ^3P_1$ transition in the room-temperature mercury vapor cell. Five Doppler-broadened profiles of the mercury isotopes with sub-Doppler Lamb dips are visible. At room temperature, the Doppler-broadened profiles are of ~ 1 GHz widths, much more than the isotopic shifts of some of the Lamb dips. The overlapping leads to situating the sub-Doppler spectral lines at the slopes, while the one for the ^{201a}Hg (shown in the inset) is the steepest.

infer the frequency value to be 1181541128(17) MHz. This value agrees with our result 118154111051(83) kHz within the uncertainty. The advent of high-power diode lasers and a non-linear frequency conversion paved the way for more precise spectroscopic measurements of mercury [18] and enabled the exploration of new areas of fundamental research based on the mercury atom [19–24]. Recently, the isotopically resolved Hg spectrum of the $^1S_0 \rightarrow ^3P_1$ intercombination transition was used for developing a new method for measuring the gaseous elemental mercury concentration in the air [25]. Our measurement enriches this spectrum with a new value, which will increase the method's accuracy.

2. Experimental setup

The experimental setup scheme is shown in Fig. 2. The laser system (Toptica TA-FHG Pro) is based on a 1016 nm laser diode in an external resonator configuration (ECDL). The power of the infrared light is amplified up to 2 W with the tapered amplifier (TA). The frequency is doubled twice, resulting in the ultraviolet 254 nm laser beam with a power of up to 120 mW. The typical laser beam intensity used in the experiment is 140 mW/cm².

To stabilize and measure the frequency of the ECDL, an optical frequency comb is used. After amplification and frequency shifting by an acousto-optic modulator (AOM1), a part of the infrared light is spatially superimposed with the comb output beam and sent to an avalanche photodiode (APD) for the frequency beat detection. The beat note signal is mixed with the RF signal from the generator (GEN) so that the frequency of the resulting signal is down-converted and adapted to the operating range of the RF counter. Its readings are used to determine the absolute frequency of infrared, and thus ultraviolet, laser light. In addition, the mixed RF signal is provided to a digital phase detector, which outputs a DC signal proportional to the phase difference between the mixed RF signal and a reference 20.5 MHz signal. The DC output signal is provided to the PID controller (Toptica FALC110), which generates a signal modulating the ECDL's current and its piezo voltage. With this approach, the infrared laser light is frequency-narrowed to about 100 kHz and locked to the optical frequency comb mode. To determine the comb mode number, a small fraction of the infrared light is guided to the wavelength meter, whose uncertainty (60 MHz)

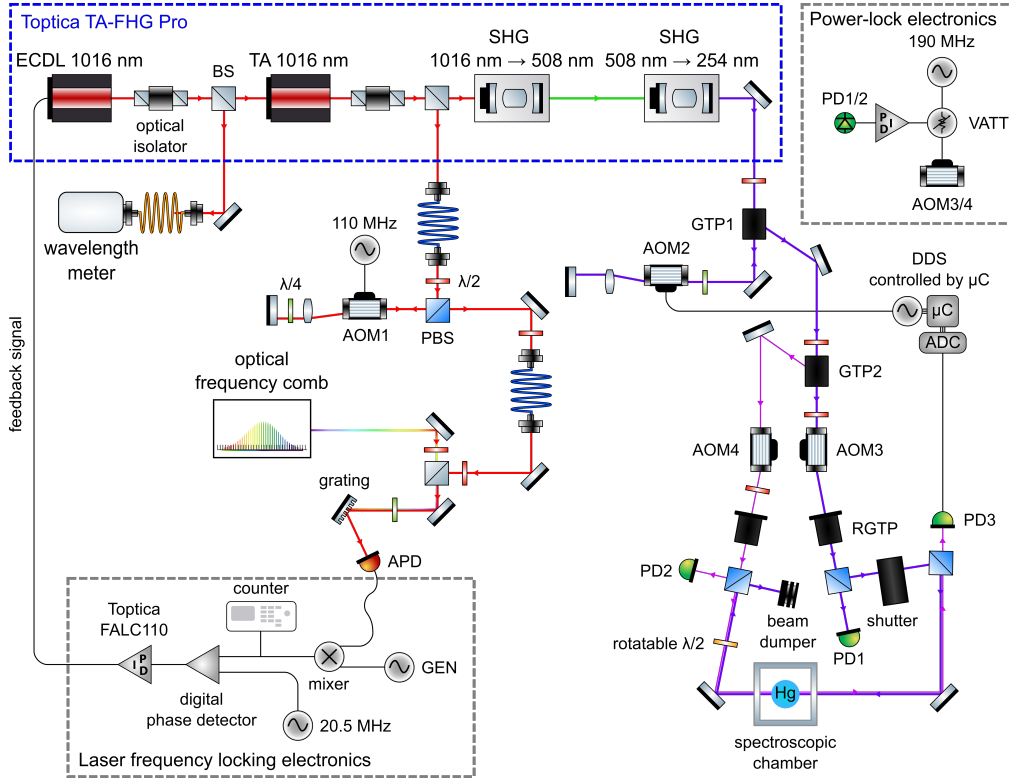


Fig. 2. Scheme of the experimental setup consisting of a laser source (Toptica TA-FHG Pro), an optical frequency comb, and a saturation spectroscopy setup. The infrared 1016 nm laser beam generated by an ECDL is referenced to the optical frequency comb. The frequency of IR light is doubled twice to obtain the UV light at a wavelength of 254 nm. The spectroscopy setup consists of a spectroscopic mercury cell, an AOM2 in double-pass configuration, and two independent power stabilization systems for the pumping and probing beams.

is a few times smaller than the comb repetition frequency (250 MHz).

Ultraviolet light is sent to the spectroscopy system. Using the saturation effect of the atomic transition [26], a sub-Doppler Lamb dip is observed. While the spectral line is free from the Doppler broadening, its width is a few times larger than the natural linewidth due to power broadening, transient-time broadening, and pressure broadening. The spectroscopy signal is used as an input of the frequency stabilization system, which tunes the UV frequency to the center of the atomic line. The frequency shifting is realized with an acousto-optic modulator (AOM2), whose RF driving signal is generated by a μC -operated direct digital synthesizer (DDS). The UV frequency-shifted beam is separated with a Glan-Taylor prism (GTP1) and split into another two beams by using the prism (GTP2). These two beams act as the pumping and probing beams in the spectroscopy system. Their power ratio can be chosen with a half-wave plate in front of the GTP2. We applied both beams' independent power-lock systems with PD1 and PD2 to ensure good power stability. For typical experimental conditions, the relative power stability is at the level of 8.3 ppm and 6.5 ppm for the pumping and probing beam, respectively. To eliminate the influence of the Doppler background, we periodically block the pumping beam, which disables the saturation of the atomic transition and measure the background level, which is then digitally subtracted. Pumping and probing beams are sent through AR-coated wedged

fused silica windows to a 1 mm thick cylindrical absorption cell containing Hg vapors. The cell is attached to a servo that allows its rotation, thus changing the length of the optical path of the probe beam inside the cell. The saturated absorption spectroscopy signal is detected with a photodiode (PD3) and sent to the microcontroller, where the UV frequency correction is calculated (see section 3).

To account for the influence of the Zeeman effect and collision-induced shifts, the spectroscopic cell was placed inside a spectroscopic chamber shown in Fig. 3. The chamber enables thermal

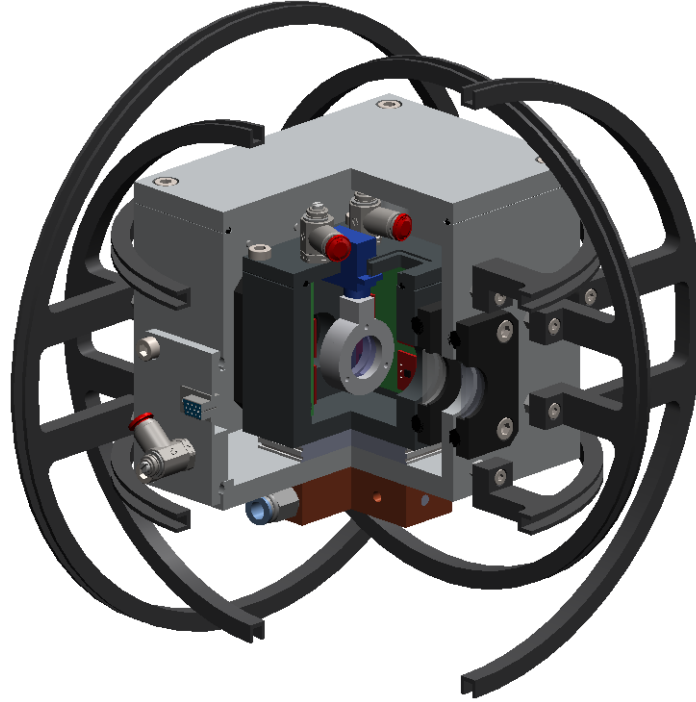


Fig. 3. Quarter-section of the spectroscopic chamber design. Two aluminum chambers surround the spectroscopic. The temperature stabilization is realized with two Peltier modules below the inner chamber. The excessive heat is removed from the system by coolant flowing through a copper plate. The cell is surrounded by eight offset-compensated 3-axis magnetometers enabling magnetic field and magnetic gradient measurements. The chamber is equipped with six coils in three independent Helmholtz arrangements to compensate for a stray magnetic field. UV light passes through the chamber via four AR-coated wedged fused silica windows.

stabilization at the level of 0.1 °C. The temperature reading is based on a measurement of a Pt100's resistance with the use of an analog-digital converter. The model used for translating the resistance into the temperature extends its uncertainty to 0.5 °C. The chamber is equipped with three pairs of coils in Helmholtz configuration to compensate for a stray magnetic field. Eight 3-axis offset-compensated magnetometers distributed around the cell enable both magnetic field strength (with the uncertainty of a few μT) and magnetic gradient measurements.

The whole spectroscopic chamber consists of two aluminum chambers: the inner and the outer one depicted in Fig. 3 in grey and silver, respectively. The volume between the inner and outer chambers is pumped out to improve thermal insulation. The inner chamber is filled with nitrogen, preventing unwanted water condensation or freezing during chamber cooling.

The temperature stabilization is realized with two Peltier modules below the inner chamber.

The excessive heat is removed through the water-cooled copper plate. The temperature of the inner chamber is measured using a Pt100 temperature sensor attached to its wall. This provides feedback to the PI controller.

3. Method

To account for the background-induced frequency shift, we improved a digital lock method (DLM), which has proven to work very well for symmetric spectral lines [18, 27, 28]. The scheme of this method is shown in Fig. 4. The DLM is based on cyclical switching of the laser frequency between

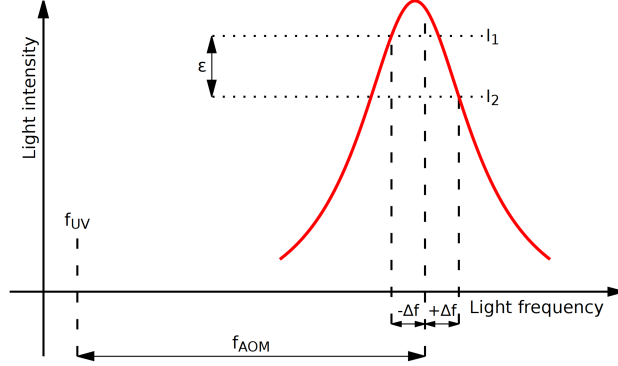


Fig. 4. Scheme of the DLM. The frequency of the laser light is shifted cyclically by Δf towards lower and higher values corresponding to the opposite slopes of the sub-Doppler spectral line obtained with the pumping beam enabled. After each frequency jump, the spectroscopic signal is measured, and the difference between two consecutive values $\varepsilon = I_1 - I_2$ is used to calculate the frequency correction by which the f_{AOM} is shifted after each cycle.

two values $f_{UV} + f_{AOM} - \Delta f$ and $f_{UV} + f_{AOM} + \Delta f$, which are related to opposite slopes of a measured line. After each frequency jump, the spectroscopy signal I is measured by a photodiode. The difference between two consecutive values ($\varepsilon = I_1 - I_2 = I_{f_{UV}+f_{AOM}-\Delta f} - I_{f_{UV}+f_{AOM}+\Delta f}$) is used to calculate the frequency correction f_{corr}

$$f_{corr} = (I_{f_{UV}+f_{AOM}-\Delta f} - I_{f_{UV}+f_{AOM}+\Delta f}) \cdot \text{gain}, \quad (1)$$

by which the f_{AOM} is shifted after each cycle. The μC calculates the frequency correction after every two frequency jumps. For the symmetric line, the laser frequency lying exactly at the center of the measured profile results in $\varepsilon = 0$, thus also $f_{corr} = 0$. With this loop, the laser frequency ($f_{UV} + f_{AOM}$) follows the spectral line's maximum position.

The DLM works very well for symmetrical profile. However, it may lie on a slope when a spectral line shares a Doppler-broadened absorption profile with other spectral lines, such as those from other isotopes. The steeper the slope, the more systematic error will be introduced by the DLM (we describe this effect in detail in section 5). To solve this issue, we developed the modified digital lock method (mDLM). The scheme of the mDLM is depicted in Fig. 5. As a significant improvement, we introduced the on-the-fly background-eliminating scheme based on disabling the saturation of the atomic transition. It is managed by repeating the frequency jumping cycle with the blocked pumping beam. Once the pumping beam is disabled, the Lamb dip disappears, and only the Doppler-broadened absorption profile remains. The cycle of two frequency jumps and signal measurements is repeated, but this time it corresponds only to the background levels, subtracted from the previously obtained spectral line measurements. As a

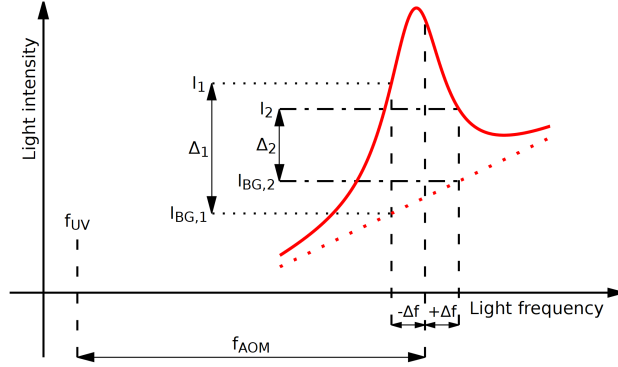


Fig. 5. Scheme of the mDLM. At the beginning of the cycle, the pumping beam is disabled, and the background-only measurement (dashed red line) is performed at $f_{UV} + f_{AOM} \pm \Delta f$, giving $I_{BG,1}, I_{BG,2}$. Then, the pumping beam is switched on and the spectroscopic signal of the sub-Doppler spectral line (solid red line) is measured for the same frequencies, giving I_1 and I_2 . The differences $\Delta_1 = I_1 - I_{BG,1}$ and $\Delta_2 = I_2 - I_{BG,2}$ are used to calculate the frequency correction by which the f_{AOM} is shifted.

result, we get two values $I_{BG,1}, I_{BG,2}$ related to the opposite background-free slopes and use them to calculate the frequency correction f_{corr}

$$f_{corr} = (\Delta_1 - \Delta_2) \cdot \text{gain}, \quad (2)$$

where

$$\begin{aligned} \Delta_1 &= I_1 - I_{BG,1} = I_{f_{UV}+f_{AOM}-\Delta f}^{\text{line+bg}} - I_{f_{UV}+f_{AOM}-\Delta f}^{\text{bg}}, \\ \Delta_2 &= I_2 - I_{BG,2} = I_{f_{UV}+f_{AOM}+\Delta f}^{\text{line+bg}} - I_{f_{UV}+f_{AOM}+\Delta f}^{\text{bg}}. \end{aligned}$$

The $I^{\text{line+bg}}$ and I^{bg} correspond to the values measured in the presence and absence of the pumping beam, respectively.

Switching off the pumping beam is accomplished with a mechanical shutter controlled by a TTL signal from the μC . The full-closing time of the shutter is 5 ms. The time frame of the entire measurement cycle of the mDLM is shown in Fig. 6

4. Microcontroller and direct digital synthesizer

A home-made digital device (Fig. 7) consisting of a direct digital synthesizer Analog Devices AD9959 evaluation board (DDS) and a Kamami ZL26ARM evaluation board with an STM32F107 microcontroller (μC) were used to precisely control the frequency of the RF signal supplied to the acousto-optical modulator and to implement the frequency correction algorithm described in section 3. The reference clock for DDS is a 100 MHz signal coming from UTC (AOS) [29, 30]. The DDS includes four output RF channels digitally tunable from 0 MHz to 210 MHz with around 100 mHz resolution. All DDS parameters are set by the μC through the SPI interface, allowing the output frequency to be switched in a microsecond which is negligible compared to the cycle time. The opening and closing of the shutter are controlled by the TTL signal from the μC digital output. The signal is sent to the TTL input of the shutter driver.

The signal from the photodetector (PD3 in Fig. 2) is measured using a 12-bit ADC converter built in the μC . The reading from the photodiode is averaged over the multiple measurements (about a thousand points per 1 ms) to improve the signal-to-noise ratio.

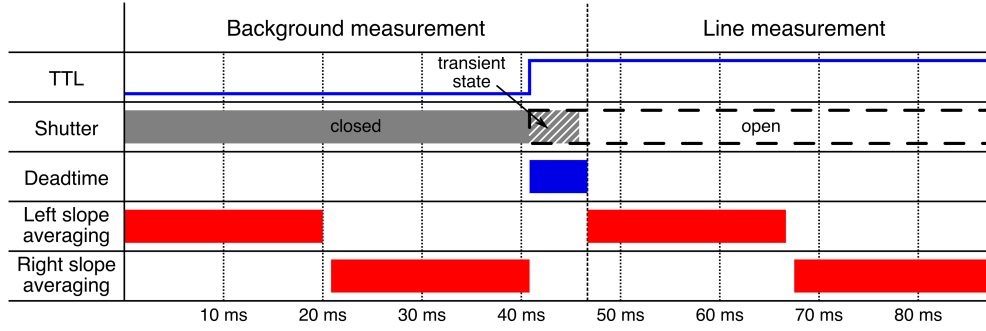


Fig. 6. The time frame of the mDLM. At the beginning of the cycle, the shutter is closed, and the background level measurements are performed consecutively for the left and right slopes of the spectral line. Next, the μ C sends the opening signal to the shutter controller. The full-opening time is 5 ms. Once the shutter is fully opened, the spectral line measurements are performed, and the frequency correction is calculated and applied. Afterward, the shutter is closed, and the cycle is repeated.

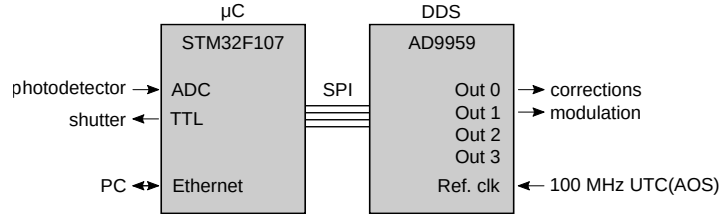


Fig. 7. Scheme of the digital device for background-free spectroscopy control. The microcontroller executes the frequency correction algorithm and communicates with peripheral devices: ADC - analog-digital converter for measuring the signal from the photodetector, DDS - direct digital synthesizer for precise frequency control of AOMs, digital ports for sending TTL signals, e.g., to the shutter. Ethernet communication acts as a user interface with the device.

The digital background-free locking algorithm is implemented in a μ C program written in C language. The program can also be switched to the background-free or background-included scan mode to observe the line profile and determine the initial lock parameters. All parameters of the μ C operation are set through commands sent via the Ethernet network. The μ C can also save user-selected parameters and measurements and share them via Ethernet.

5. Background-induced systematic shift

If the separation of the spectral lines is small compared to their Doppler widths, the absorption profiles overlap, and the associated Lamb dips are no longer situated at the profile center but on the slope. Consequently, the peak of the Lamb dip is frequency-shifted according to the atomic resonant frequency. To analyze this shift, we model the measured atomic transition as a Lorentz profile with a linear background. The latter is justified since the width of the Doppler-broadened absorption profile is much larger than the linewidth of the atomic transition. The observed spectral line intensity profile can be then written as

$$I(f) = \frac{A}{1 + \left[\frac{2(f-f_0)}{w} \right]^2} + a(f-f_0) + b, \quad (3)$$

where A and w are the amplitude and the width of the Lorentz profile, respectively, $f - f_0$ is the detuning from the atomic resonant frequency, and a , together with b , is the linear slope parameters. In the case of the DLM, the value f_{DLM} at which the light frequency is stabilized does not correspond to the resonant frequency f_0 of the atomic transition but is shifted instead. Moreover, this shift depends on the jumps magnitude Δf in the frequency correction cycles. To calculate the frequency shift ($f_{\text{DLM}} - f_0$) as a function of Δf , one can solve the equation

$$I(f + \Delta f) = I(f - \Delta f), \quad (4)$$

which can be reduced to

$$\alpha_5(f - f_0)^4 + \alpha_3(f - f_0)^2 + \alpha_2(f - f_0) + \alpha_1 = 0, \quad (5)$$

where

$$\begin{aligned} \alpha_5 &= 16, \\ \alpha_3 &= 8w^2 - 32\Delta f^2, \\ \alpha_2 &= -\frac{8w^2A}{a}, \\ \alpha_1 &= w^4 + 8w^2\Delta f^2 + 16\Delta f^4. \end{aligned}$$

The dependence of the frequency f_{DLM} satisfying the Eq. (4) on Δf is elaborate but for $\Delta f < w$ can be approximated as

$$f_{\text{DLM}}(\Delta f) = \beta_4(\Delta f)^4 + \beta_2(\Delta f)^2 + \beta_1, \quad (6)$$

where β_i consist of the profile and slope parameters.

The background introduces a systematic error that cannot be avoided within DLM, even with infinitesimally small frequency jumps Δf . The mDLM solves this issue as the spectral line with the slope background (Fig. 8) is seen to be symmetric due to on-the-fly background subtracting

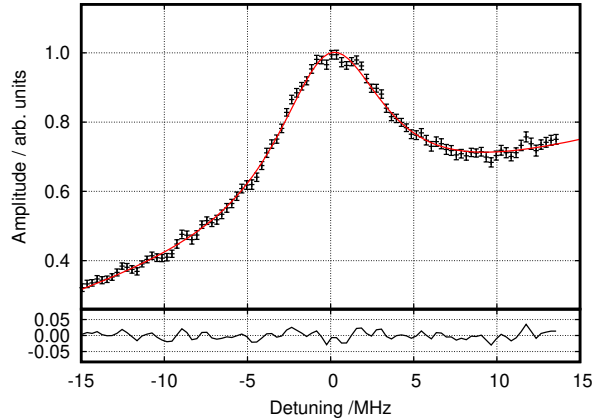


Fig. 8. Sub-Doppler spectral line profile obtained with the saturation spectroscopy of the $^1S_0 \rightarrow ^3P_1$ transition in ^{201}aHg . This line is situated on the slope arising from sharing the Doppler-broadened absorption profile with neighboring ^{199}aHg and ^{204}Hg spectral lines. The results are averaged over fifteen scans and fit according to Eq. 3. The bottom part of the figure shows the residuals.

(Fig. 9). To validate the equation (6), the dependence of the frequency at which the laser light was

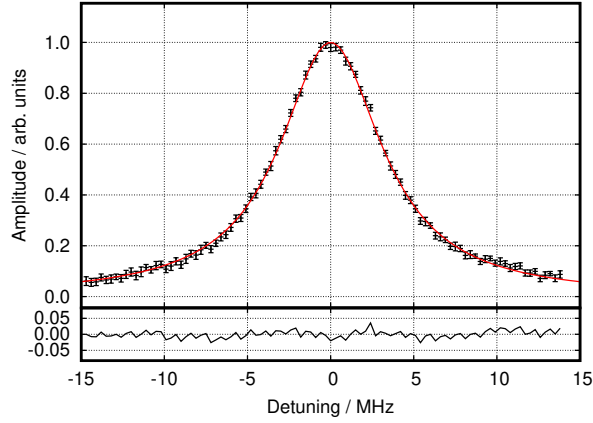


Fig. 9. Sub-Doppler spectral line profile obtained with the saturation spectroscopy of the $^1S_0 \rightarrow ^3P_1$ transition in ^{201}Hg with linear background subtracted on-the-fly by the μC . Subtracting the background makes the spectral line seen as symmetric. The results are averaged over fifteen scans and fit with the Lorentzian profile. The bottom part of the figure shows the residuals.

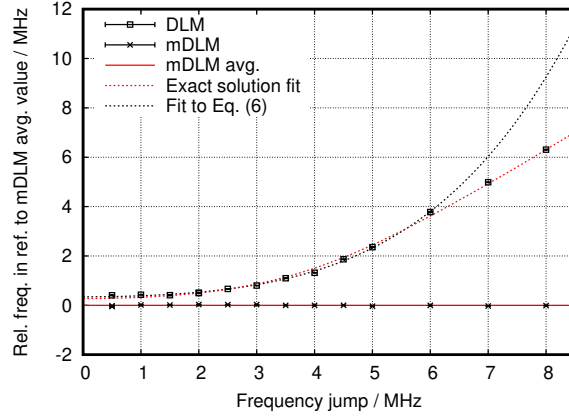


Fig. 10. Dependence of the relative frequency at which the laser light was stabilized on Δf in reference to mDLM average value (solid red line). Square points (DLM) are fit according to Eq. (6) (dashed black line) and to the solution of Eq. (4) (dashed red line). The mDLM results (cross points) do not depend on the Δf .

stabilized as a function of the frequency jump Δf was measured for DLM and mDLM (Fig. 10) with the $^1S_0 \rightarrow ^3P_1$ ^{201}Hg transition.

For the DLM, unlike the mDLM case, the frequency value shifts rapidly with the frequency jump. Moreover, even for a small Δf , the discrepancy $\Delta_{\text{DLM-mDLM}}$ between results obtained with both methods persists. In general, this deviation depends on the ratio a/A and the linewidth w . Typically, $\Delta_{\text{DLM-mDLM}}$ is much smaller than the linewidth. Hence, for the Lorentzian profile, the deviation can be approximated as

$$\Delta_{\text{DLM-mDLM}} \approx \frac{aw^2}{8A}. \quad (7)$$

For our specific experimental conditions, the discrepancy shown in Fig. (10) is of 280 kHz.

6. μ C software parameters

In the mDLM, the frequency correction f_{corr} is calculated by the μ C according to equation (2). The gain has to be adjusted accordingly to ensure the frequency correction is fast enough to keep up with the frequency drifts of the spectral line and the laser light. Fig. 11 shows the dependence

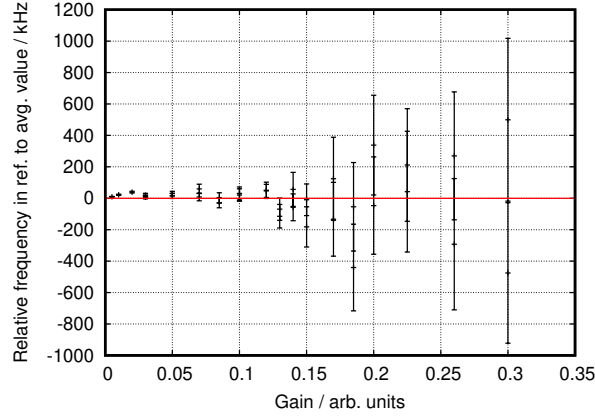


Fig. 11. Dependence of the relative frequency at which the laser light was stabilized on the gain in reference to the mDLM average value (solid line). For high gain, the frequency corrections are too extensive, causing big uncertainties. Too low gains make the system unable to keep up with the frequency drifts of the laser light.

of the frequency at which the laser light was stabilized on the gain. For high gain, the frequency correction f_{corr} is too extensive, which leads to high uncertainties. Too small gain makes the system unable to keep up with the frequency drifts, which results in scattering the results in the tens of kHz range.

As shown in Fig. 10, in the mDLM the frequency at which the laser light stabilizes does not depend on the frequency jump Δf . Despite this, the parameter Δf should be adjusted according to the spectral linewidth w . For the optimal frequency jump, the sensitivity of the mDLM is the highest. This is the case for the steepest parts of the slopes being probed. It corresponds to the maximum of the first derivative of the spectral line profile. For the Lorentzian profile, the optimal $\Delta f = w/\sqrt{12}$. For this specific value, the deviation of the laser frequency from the spectral line's resonance results in the largest response of the correction system, shown in Fig. 12.

7. Absolute frequency

To validate the mDLM performance, we used it to determine the absolute frequency of the $^1S_0 \rightarrow ^3P_1$ transition in ^{201}Hg ($F = 3/2 \rightarrow F' = 5/2$), located on the steepest slope of the Doppler profile among all Hg isotopes at room temperature. The determined absolute frequency is 1181541111051(83) kHz. To obtain this value, the optical frequency comb was used and the error budget was measured. The total uncertainty was calculated according to the following formula

$$u(f_{\text{abs}}) = \sqrt{u_{\text{stat}}^2 + u(\Delta_{\text{AC-Stark}})^2 + u(\Delta_{\text{Hg-Hg}})^2 + u(\Delta_{\text{Hg-H}_2})^2 + \sum_{i=1}^3 u(\Delta_{\text{Zeeman-}i})^2}, \quad (8)$$

where $u_{\text{stat}} = 3.9$ kHz is the statistical uncertainty of the line position measured under known and controllable experimental conditions, $\Delta_{\text{AC-Stark}}$ is the AC-Stark frequency shift, $\Delta_{\text{Hg-Hg}}$ and $\Delta_{\text{Hg-H}_2}$ are the pressure shifts, and $\Delta_{\text{Zeeman-}i}$ are Zeeman shifts of the x , y , and z -axis, respectively. All the components are described in the following subsections and the values are summarized in Table 1.

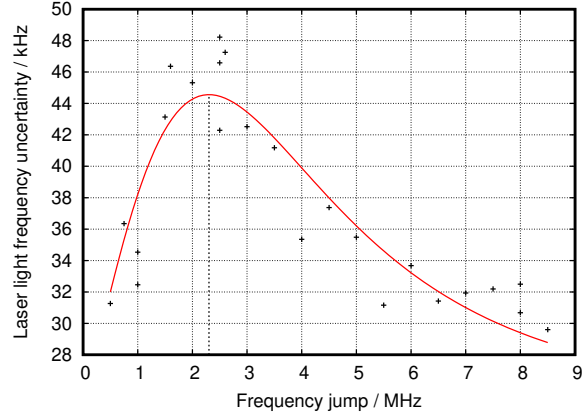


Fig. 12. Dependence of the laser light stabilizing frequency uncertainty on the frequency jump. The first derivative of a Lorentz profile is fit to the collected data. The maximum of the fit corresponds to the $\Delta f = w/\sqrt{12}$ (dashed line), at which the mDLM sensitivity is the highest.

7.1. AC-Stark shift

The energy levels of the atoms are shifted under the influence of the electric field of the laser beam. To estimate the contribution of this effect, we measured the position of the spectral line for different UV light power (Fig. 13). A linear fit weighted by the points' uncertainties yields the AC-Stark shift correction factor of $-148.6(9.4)$ kHz/mW.

The uncertainties are mainly related to the accuracy of the power meter used (Thorlabs S130VC) and the power measuring method. The total uncertainty is deduced to be 5.4%.

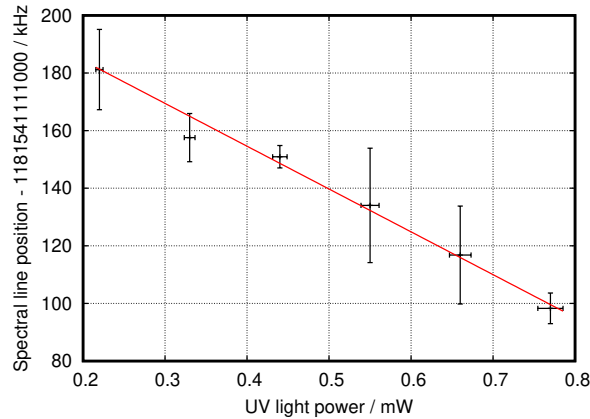


Fig. 13. Dependence of the spectral line position on the total power of the UV beams. The solid red line is a weighted fit to the results. The AC-Stark shift is deduced from the slope to be $-148.6(9.4)$ kHz/mW.

7.2. Pressure shift

The pressure-dependent collisions between Hg atoms and residual gases affect the atomic transition frequency. Since the vapor pressure of Hg depends on the temperature, the spectroscopic cell temperature was actively stabilized. The average temperature of the cell during measurements

was 19.97(50) °C, which corresponds to 0.1708(75) Pa vapor pressure [31]. The temperature uncertainty is limited by the accuracy of the analog-digital converter used in the Pt100-based temperature measurement scheme.

We used the same approach as presented in [18] to estimate a collision-induced shift. The collisions between mercury atoms shift the transition frequency by $-22(22)$ kHz/Pa. The contribution from the collisions with residual gases was estimated, assuming molecular hydrogen as a dominant component, which is consistent with the fused silica cell residual gases composition [32]. H_2 pressure at room temperature is less than 0.13 Pa, corresponding to the spectral line shift of $-35(35)$ kHz/Pa.

7.3. Zeeman shift

The ^{201}Hg isotope (abundance of 13.18% [33]) is a fermion with non-zero nuclear spin ($I = 3/2$), which leads to hyperfine splitting of the 3P_1 state into three states ($F = 5/2, 3/2, 1/2$) [34]. The $F = 3/2 \rightarrow F' = 5/2$ transition is the measured one. The ground state $^1S_0, F = 3/2$ splitting is negligible in a weak magnetic field as the nuclear Landé factor is much smaller than the orbital and the electron ones. The excited state $^3P_1, F = 5/2$ splits into six substates characterized by magnetic quantum number m_F . To a first approximation, the linear Zeeman effect splits the sublevels symmetrically and therefore has no contribution to the absolute frequency shift. On the other hand, the quadratic Zeeman effect does not cause splitting but can produce a non-negligible shift of the hyperfine levels.

To estimate the Zeeman shift, the spectral line position was independently measured for different magnetic fields for each axis. The external magnetic field of the Helmholtz coils was varied over a range that did not split the spectral line measurably. The results corresponding to the vertical (x -axis, Fig. 14) and horizontal (z -axis, Fig. 15), both perpendicular to the UV beams, manifest significant quadratic and linear Zeeman effects. For the axial magnetic field component

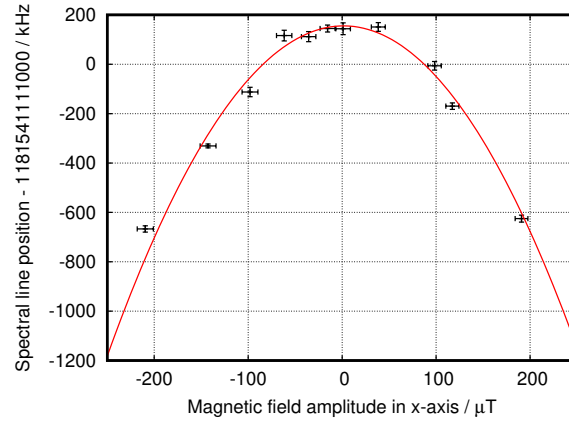


Fig. 14. Dependence of the spectral line position on the magnetic field in the x -axis (vertical, perpendicular to the UV beams). The solid red curve is a weighted parabola fit to the results. The quadratic and linear Zeeman shifts are deduced to be $-0.0211(13)$ kHz/ μT^2 and $0.07(16)$ kHz/ μT , respectively.

(Fig. 16), a very large shift, which exhibits only a linear dependence in the measured range, is observed. The magnetic field was measured by eight 3-axis offset-compensated magnetometers located symmetrically around the spectroscopic cell. Each reading has an uncertainty related to the accuracy of the offset calibration. Each point in the graphs corresponds to the average value of the magnetometers' readings for a given axis. The variance of the readings specifies the uncertainties of the points.

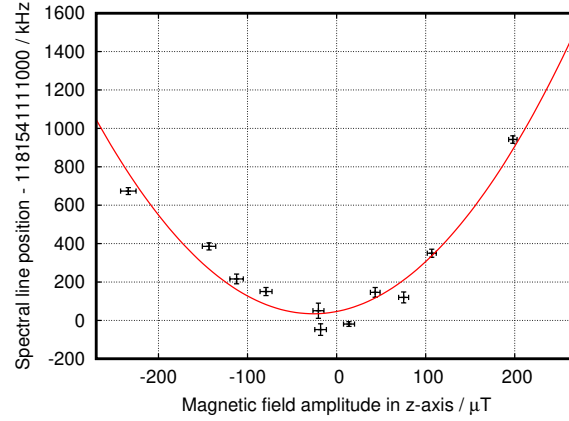


Fig. 15. Dependence of the spectral line position on the magnetic field in the z-axis (horizontal, perpendicular to the UV beams). The solid red curve is a weighted fit to the results. The quadratic and linear Zeeman shifts are deduced to be $0.0170(15) \text{ kHz}/\mu\text{T}^2$ and $0.89(22) \text{ kHz}/\mu\text{T}$, respectively.

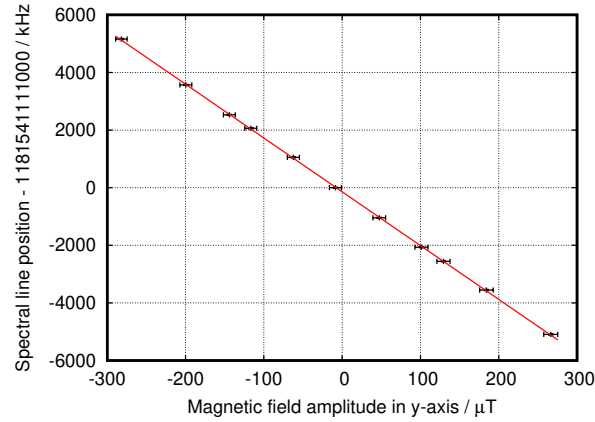


Fig. 16. Dependence of the spectral line position on the magnetic field in the y-axis (along UV beams). The solid red line is a weighted fit to the results. The linear Zeeman shift is deduced to be $-18.677(53) \text{ kHz}/\mu\text{T}$

To account for the Zeeman effect, the magnetic field and its gradient were measured during the absolute frequency measurement. The uncertainty-weighted sensors' readings were averaged, resulting in six magnetic field values, one for each side of the spectroscopic cell. The uncertainty of these results was deduced from the calculated internal and external variances, where the larger of the two was chosen. The average of pairs of points along the same axis determines the value of the magnetic field at the center of the spectroscopic cell, which was calculated to be $43.6(3.6) \mu\text{T}$, $-11.6(4.3) \mu\text{T}$, and $-7.46(0.77) \mu\text{T}$ for x, y, and z-axis, respectively.

8. Conclusions

In summary, we demonstrated a novel method to stabilize the frequency of laser light on the position of a spectral line. The method is especially beneficial in the case of the atomic lines located on the slope of the absorption profile, which induces a systematic frequency shift. We derived a formula to calculate the background-induced shift, which was then compared with the

Table 1. Systematic shifts and their uncertainties determined for the experimental conditions, i.e., UV beams total power of 0.440(24) mW, spectroscopic cell temperature of 19.97(50) °C, and magnetic field of 43.6(3.6) μ T, $-11.6(4.3)$ μ T and $-7.46(0.77)$ μ T for x, y, and z-axis respectively. All results are in kHz.

Effect					
AC-Stark	Pr. shift Hg-Hg	Pr. shift Hg-H ₂	Zeeman x-axis	Zeeman y-axis	Zeeman z-axis
65.4(5.4)	3.8(3.8)	4.6(4.6)	37.1(9.8)	-217(80)	5.7(1.7)

experimental results, showing full agreement. To demonstrate the performance of our method, we performed a measurement of the absolute frequency of the $^1S_0 \rightarrow ^3P_1$ ^{201}aHg improving the accuracy by three orders of magnitude. Our result agrees with the previously measured value within the uncertainty.

Funding

Narodowe Centrum Nauki (2021/42/E/ST2/00046, 2021/41/B/ST2/00681); European Metrology Programme for Innovation and Research (20FUN01 TSCAC).

Acknowledgments

This project 20FUN01 TSCAC has received funding from the EMPIR programme co-financed by the Participating States and from the European Union’s Horizon 2020 research and innovation programme. This work was supported by the National Science Centre, Poland Project no. 2021/42/E/ST2/00046. A. Linek is supported by the National Science Centre, Poland, Project no. 2021/41/B/ST2/00681.

The measurements were performed as a part of research done at the National Laboratory FAMO (KL FAMO) in Toruń, Poland. KL FAMO in Toruń is supported by the subsidy of the Ministry of Science and Higher Education. The authors would like to thank Roman Ciuryło for fruitful discussions. The authors also thank Mode-Locked Technology Sp. z o.o. for providing the digital phase detector for laser frequency stabilization.

Disclosures

The authors declare no conflicts of interest.

Data availability

Data underlying the results presented in this paper are available in the open data repository [35].

References

1. R. K. Raj, D. Bloch, J. J. Snyder, G. Camy, and M. Ducloy, “High-Frequency Optically Heterodyned Saturation Spectroscopy Via Resonant Degenerate Four-Wave Mixing,” *Phys. Rev. Lett.* **44**, 1251–1254 (1980).
2. G. C. Bjorklund, “Frequency-modulation spectroscopy: a new method for measuring weak absorptions and dispersions,” *Opt. Lett.* **5**, 15–17 (1980).
3. J. E. Debs, N. P. Robins, A. Lance, M. B. Kruger, and J. D. Close, “Piezo-locking a diode laser with saturated absorption spectroscopy,” *Appl. Opt.* **47**, 5163–5166 (2008).
4. E. van Ooijen, G. Katgert, and P. van der Straten, “Laser frequency stabilization using Doppler-free bichromatic spectroscopy,” *Appl. Phys. B* **79**, 57–59 (2004).
5. G. Wasik, W. Gawlik, J. Zachorowski, and W. Zawadzki, “Laser frequency stabilization by Doppler-free magnetic dichroism,” *Appl. Phys. B* **75**, 613–619 (2002).
6. L. Krzemień, K. Brzozowski, A. Noga, M. Witkowski, J. Zachorowski, M. Zawada, and W. Gawlik, “Laser frequency stabilization by magnetically assisted rotation spectroscopy,” *Opt. Commun.* **284**, 1247–1253 (2011).
7. M. Aldous, J. R. C. Woods, A. Dragomir, R. Roy, and M. Himsworth, “Carrier frequency modulation of an acousto-optic modulator for laser stabilization,” *Opt. express* **25** **11**, 12830–12838 (2017).
8. H. Kayser and C. Runge, “Ueber die Spectra der Elemente der zweiten Mendelejeff’schen Gruppe,” *Annalen der Physik* **279**(6), 385–409 (1891).
9. C. E. Moore, *Atomic Energy Levels*, vol. 3 (U.S. Government Printing Office, 1958).

10. C. V. Stager and R. H. Kohler, "Hyperfine structure of Hg^{199} and Hg^{201} in the $^3\text{P}_1$ state," *Bull. Am. Phys. Soc. Ser. II* **5**(4), 274 (1960).
11. W. G. Schweitzer, "Hyperfine structure and isotope shifts in the 2537-Å line of mercury by a new interferometric method," *J. Opt. Soc. Am.* **53**(9), 1055–1072 (1963).
12. J. Reader, C. H. Corliss, W. L. Wiese, and G. A. Martin, *Wavelengths and transition probabilities for atoms and atomic ion* (U.S. Government Printing Office, 1980).
13. R. H. Kohler, "Detection of double resonance by frequency change: application to Hg^{201} ," *Phys. Rev.* **121**(4), 1104–1111 (1961).
14. E. B. Saloman, "Wavelengths, energy level classifications, and energy levels for the spectrum of neutral mercury," *J. Phys. Chem. Ref. Data* **35**(4), 1519–1548 (2006).
15. C. J. Sansonetti and D. Veza, "Doppler-free measurement of the 546 nm line of mercury," *J. Phys. B: At. Mol. Opt. Phys.* **43**, 205003 (2010).
16. A. E. Kramida, "Re-optimized energy levels and Ritz wavelengths of (198)Hg I," *J. Res. Natl. Inst. Stand. Technol.* **116**(2), 599–619 (2011).
17. W. G. Schweitzer, "Wavelength Passed by Hg^{198} Zeeman-Split Absorption Filter," *J. Opt. Soc. Am.* **53**(9), 1250–1252 (1963).
18. M. Witkowski, G. Kowzan, R. Munoz-Rodriguez, R. Ciuryło, P. S. Żuchowski, P. Masłowski, and M. Zawada, "Absolute frequency and isotope shift measurements of mercury 1S0-3P1 transition," *Opt. Express* **27**, 11069–11083 (2019).
19. M. S. Safronova, D. Budker, D. DeMille, D. F. J. Kimball, A. Derevianko, and C. W. Clark, "Search for new physics with atoms and molecules," *Rev. Mod. Phys.* **90**, 025008 (2018).
20. C. Bouchiat, "Parity violation in atomic processes," *J. Phys. G: Nucl. Phys.* **3**(2), 183–197 (1977).
21. K. V. P. Latha, D. Angom, B. P. Das, and D. Mukherjee, "Probing CP violation with the electric dipole moment of atomic mercury," *Phys. Rev. Lett.* **103**, 083001 (2009).
22. M. D. Swallows, T. H. Loftus, W. C. Griffith, B. R. Heckel, E. N. Fortson, and M. V. Romalis, "Techniques used to search for a permanent electric dipole moment of the ^{199}Hg atom and the implications for CP violation," *Phys. Rev. A* **87**, 012102 (2013).
23. B. Graner, Y. Chen, E. G. Lindahl, and B. R. Heckel, "Reduced limit on the permanent electric dipole moment of ^{199}Hg ," *Phys. Rev. Lett.* **116**, 161601 (2016).
24. E. J. Angstrom, V. A. Dzuba, and V. V. Flambaum, "Relativistic effects in two valence-electron atoms and ions and the search for variation of the fine-structure constant," *Phys. Rev. A* **70**, 014102 (2004).
25. A. Srivastava and J. T. Hodges, "Development of a High-Resolution Laser Absorption Spectroscopy Method with Application to the Determination of Absolute Concentration of Gaseous Elemental Mercury in Air," *Anal. Chem.* **90**, 8781–8788 (2018).
26. D. W. Preston, "Doppler-free saturated absorption: Laser spectroscopy," *Am. J. Phys.* **64** (1996).
27. P. Morzyński, P. Wcisło, P. Ablewski, R. Gartman, W. Gawlik, P. Masłowski, B. Nagórny, F. Ozimek, C. Radzewicz, M. Witkowski, R. Ciuryło, and M. Zawada, "Absolute frequency measurement of rubidium 5S-7S two-photon transitions," *Opt. Lett.* **38**, 4581–4584 (2013).
28. P. Morzyński, P. Wcisło, P. Ablewski, R. Gartman, W. Gawlik, P. Masłowski, B. Nagórny, F. Ozimek, C. Radzewicz, M. Witkowski, R. Ciuryło, and M. Zawada, "Line shape measurements of rubidium 5S-7S two-photon transition," *J. Phys. Conf. Ser.* **548**, 012023 (2014).
29. J. Azoubib, J. Nawrocki, and W. Lewandowski, "Independent atomic timescale in Poland—organization and results," *Metrologia* **40**, S245–S248 (2003).
30. Z. Jiang, A. Czuba, J. Nawrocki, W. Lewandowski, and F. Arias, "Comparing a gps time link calibration with an optical fibre self-calibration with 200 ps accuracy," *Metrologia* **52** (2015).
31. M. L. Huber, A. Laesecke, and D. G. Friend, "Correlation for the vapor pressure of mercury," *Ind. Eng. Chem. Res.* **45**, 7351–7361 (2006).
32. W. Palosz, "Residual gas in closed systems-I: development of gas in fused silica ampoules," *J. Cryst. Growth* **267**, 475–483 (2004).
33. J. K. Böhlke, J. R. de Laeter, P. D. Bièvre, H. Hidaka, H. S. Peiser, K. J. R. Rosman, and P. D. P. Taylor, "Isotopic compositions of the elements, 2001," *J. Phys. Chem. Ref. Data* **34**, 57–67 (2005).
34. T. Bernd, "Optical mercury magnetometry for fundamental physics experiments," *Dissertation, Technische Universität München, München* (2018).
35. M. Witkowski, A. Linek, and P. Morzyński, "Absolute frequency measurement of the $6s2\ 1S0 \rightarrow 6s6p\ 3P1\ F = 3/2 \rightarrow F' = 5/2$ ^{201}Hg transition with background-free saturation spectroscopy," (2022). <https://doi.org/10.18150/PJIBRO>.